PHYSICAL REVIEW B **102**, 214429 (2020)

Unconventional domain-wall pairs and interacting Bloch lines in a Dzyaloshinskii-Moriya multilayer thin film

Joseph A. Garlow,[1,2] Marco Beleggia,[3] Shawn D. Pollard,[4] Hyunsoo Yang,[4] and Yimei Zhu[1,2,*]
[1]*Condensed Matter Physics and Materials Science Division, Brookhaven National Laboratory, Upton, New York 11973, USA*
[2]*Department of Materials Science and Chemical Engineering, Stony Brook University, Stony Brook, New York 11794, USA*
[3]*DTU Nanolab, Technical University of Denmark, 2800 Kgs. Lyngby, Denmark*
[4]*Department of Electrical and Computer Engineering, National University of Singapore, Singapore 117576*

(Received 26 May 2020; revised 9 October 2020; accepted 3 November 2020; published 23 December 2020;
corrected 11 January 2022)

Bloch lines (BLs) play a key role in determining the static and dynamic behavior of chiral domain walls and skyrmions in multilayer films with a significant Dzyaloshinskii-Moriya interaction (DMI). Here, using *in situ* Lorentz phase microscopy, we reveal a type of spin texture termed a type-II domain-wall pair (DWP), stabilized in DMI multilayer thin films with BLs. For a type-II DWP, the Bloch components of each complementary domain wall are parallel, implying opposite chirality. We find that type-II DWPs preferentially form through bifurcation of a type-I DWP and require the formation of at least two BLs. We demonstrate a distinct phase jump associated with type-II DWPs, and further we reveal the role they play in the formation of mixed-character skyrmions where the Bloch component can be of either left- or right-handed chirality.

DOI: 10.1103/PhysRevB.102.214429

I. INTRODUCTION

The Dzyaloshinskii-Moriya interaction (DMI) in bulk noncentrosymmetric crystals and asymmetric multilayer thin films has generated significant interest for its ability to stabilize skyrmions and chiral domain walls [1–4]. The theoretical prediction and experimental observation of discrete nanoscale skyrmions at room temperature has enabled the conceptualization of beyond-CMOS spintronic memory and logic devices where skyrmions or chiral domain walls serve as information carriers that can be efficiently displaced with electrical pulses by spin-orbit torques at high velocities in racetrack device configurations [5–10]. In such devices, the displacement of the skyrmion or domain wall is dictated by the interaction between the spin structure and spin-polarized currents, where subtle changes to the spin textures can modify the desired displacement. Yet, issues remain for the utilization of spintronic devices, including the skyrmion Hall effect, where the displacement of a skyrmion occurs with a characteristic angle away from its expected trajectory [9,11]. Creative approaches to control the skyrmion Hall effect include the use of ferrimagnetic thin films [12] and synthetic antiferromagnets [13] that have demonstrated potential for a reduction of the skyrmion Hall angle. With this present work, we seek to provide quantitative information on the topology of chiral spin structures toward the realization of racetrack device architectures.

For the advent of functional skyrmionic devices, it is imperative to fully resolve their detailed spin structure to understand local energetics and/or interactions that play a role in their creation and stability, both statically and dynamically. Of particular relevance, it has been shown analytically, numerically, and experimentally that for thick DMI films, demagnetization can be sufficient to overcome the DMI effective field and impart an achiral Bloch component to the domain wall that will play a key role in determining the skyrmion Hall angle [14–18]. The transition between right-handed and left-handed Bloch walls necessitates the formation of Bloch lines (BLs), however little is known about their structure and potential interactions experimentally.

BLs have received considerable attention due to their influences on the physics of magnetic bubbles, a previously explored pathway to gigabit memory [19–25]. Further, the use of BLs as information carriers was proposed for Bloch-line memory in the 1980s [26–30]. Recently, it was discovered that BLs play a prominent role in the magnetic and electric field induced propagation of mixed Bloch/Néel domain walls in DMI multilayer thin films [31–33]. Lemesh and Beach [31] developed an analytical model that describes a Walker-breakdown-like phenomenon in the presence of current-induced spin orbit torques that originates from complex stray field interactions for both twisted domain walls and skyrmions. Moreover, Krizakova *et al.* [32] reported that a Néel domain wall displaced by a magnetic field reaches a turbulent plateau that extends past the expected Walker breakdown due to the formation of BLs, even for perfect samples without localized defects such as grain boundaries. Their work agrees with the seminal work on the formation of BLs as the origin of the suppressed velocity reduction after the Walker field reported by Yoshimura *et al.* [33]. Finally, it has been postulated that, for DMI multilayers, BLs could also stabilize additional topological defects within the domain wall itself, termed domain-wall skyrmions, which emphasizes the need to resolve fine magnetic structure at the nanoscale [34]. Despite the relevance of BLs, little has been observed experimentally about the nature of BLs—their formation, persistence, and

---

[*] zhu@bnl.gov

their potential influence on skyrmion formation, in part due to their inherently nanoscale character, which places limitations on available experimental techniques.

Here, using *in situ* Lorentz phase microscopy, we reveal a spin configuration in DMI multilayer thin films that is termed a type-II domain wall pair (DWP), and we extend our previously developed method [17] to include the transport-of-intensity equation (TIE) as a means to map the local projected magnetic induction of complex chiral structures with fine detail. In general, DWPs are a special type of 360° domain wall, as the magnetization evolves from down (along the applied field direction), to up, to down again. They can be classified into two types: type-II, where the Bloch components of each 180° wall in the pair are parallel, implying opposite chirality, and type-I, comprised of antiparallel Bloch components with the same chirality, which may be either right- or left-handed. We find that type-II DWPs preferentially form through bifurcation of a type-I DWP, and their appearance requires the formation of at least two BLs. We establish the prevalence and evolution of type-II domain regions, and we show that the required BLs interact via their stray fields. Finally, we demonstrate that at high applied fields, type-II DWPs can lead to the formation of mixed-character skyrmions with a Bloch component that can be of either left- or right-handed chirality.

II. RESULTS AND DISCUSSION

Lorentz phase microscopy (LPM) is a powerful tool to study nanoscale magnetic topology [35–37], with the capacity to probe local spin configurations at the sub-5-nm length scales [38], and it has been previously used to visualize BLs and non-$Q = 1$ topological defects [39,40]. LPM contrast is the result of a phase shift in the electron wave as it passes through a magnetic field where the contrast at the domain wall is proportional to the component of the curl of the magnetization along the beam propagation direction in the small defocus limit [41]. Beyond Lorentz imaging, electron phase retrieval techniques, including the transport-of-intensity equation (TIE), are well-suited to map the local projected magnetic induction with nanometer resolution under ideal conditions and with special care to account for microscope specific aberrations [41–51]. A schematic of the TIE approach for the retrieval of electron phase information is shown in Fig. 1 of the Supplemental Material [52]. Phase retrieval by TIE is generally regarded as qualitative, since it requires introducing a nonzero constant, q_0, to prevent a numerical singularity in the solution of the TIE equation through Fourier methods, and filtering out low-frequency noise. Nevertheless, with careful image acquisition, analysis, and benchmarking with known structures, quantitative information can be obtained [41,48,49,51]. A demonstration of how q_0 impacts the retrieved phases, and how we can rule out the potential introduction of artifacts for type-I and type-II DWPs, can be seen in Figs. 2 and 3 of the Supplemental Material [52].

The structure of type-I and type-II DWPs is shown schematically in Fig. 1(a). The difference in alignment between the two domain walls of a pair (antiparallel in type-I and parallel in type-II) creates a notable difference in the Lorentz contrast and phase images, as also shown schematically in Fig. 1(a). For type-II the contrast from each wall is identical, whereas for type-I the contrast from one wall mirrors the other. This has a profound impact on electron phase imaging of the structures. For a type-I region, the electron phase shift across each domain wall is again a mirror of the other and results in a phase increase across one domain wall with a corresponding decrease in phase (or vice versa), thereby producing two distinct phase levels—outside the domain and within the domain. However, for a type-II region, the phase jump from each wall is of the same sign and generates additional phase levels and discrete contrast in the phase image. The difference image, phase image, and induction maps for type-I and type-II domain regions are shown in Fig. 1(d) to demonstrate their contrast as well as to serve as a reference to guide image interpretation.

A schematic of the multilayer thin film studied in this work is shown in Fig. 1(c), with further details provided in the Methods section of the Supplemental Materials [52]. To approximate the expected Fresnel contrast and phase shifts produced by type-I and type-II DWPs, micromagnetic simulations were performed using MUMAX [53]. From Fig. 1(b) it can be seen that both type-I and type-II DWPs are stable in the $N = 30$ 0.7/0.5 Co/Pd DMI multilayer thin film. Using the simulated type-I and type-II domain structures, we performed LPM simulations using MALTS [54] with conditions analogous to that of the lowest defocus value in Fig. 2. For the simulated Fresnel images, the contrast agrees qualitatively with the expected contrast shown schematically. However, for the case of the phase shift from the type-II domain that is demonstrated with a line scan, there is a phase gradient in the vicinity of the type-II domain, a result of stray fringing fields associated with type-II DWPs and their BL terminations, as emphasized in Fig. 4.

To calculate the appearance of DWPs when imaged out-of-focus, we start from the normalized magnetization vector describing a mixed-character 180° domain wall along the y-axis of a Cartesian reference system,

$$\mathbf{m}(x; w, \eta) = \left\{\sin(\eta)\operatorname{sech}\left(\frac{x}{w}\right), \cos(\eta)\operatorname{sech}\left(\frac{x}{w}\right), \tanh\left(\frac{x}{w}\right)\right\}. \tag{1}$$

The mixed-character parameter η captures the global chirality of the domain wall: when η is in the range $[0,\pi/2]$, both Bloch and Néel components are counterclockwise, when η is in the range $[\pi/2,\pi]$, the Néel component remains CCW, but the Bloch component is CW, and so forth. To construct a DWP, we superimpose two magnetization distributions as in Eq. (1) laterally displaced by an amount W, where we assume $W > 5$ w to neglect interactions, where w is the domain-wall width defined as the region over which the magnetization flips from up-to-down, or vice versa:

$$\mathbf{m}^{\mathbf{I}}(x; \mathrm{W}, w, \eta) = \mathbf{m}(x + W/2; w, \eta) + \mathbf{m}(x - W/2; w, \eta + \pi), \tag{2}$$

$$\mathbf{m}^{\mathbf{II}}(x; \mathrm{W}, w, \eta) = \mathbf{m}(x + W/2; w, \eta) + \mathbf{m}(x - W/2; w, \eta). \tag{3}$$

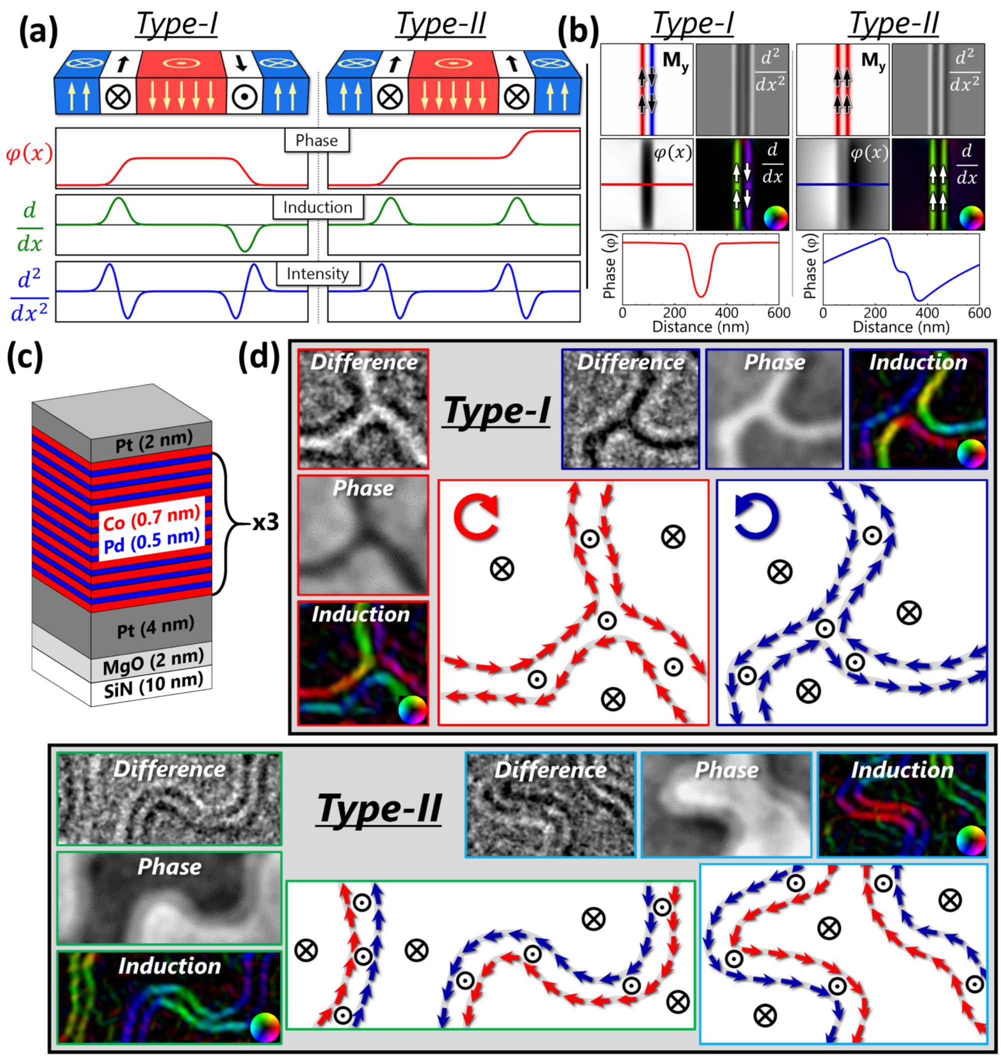

FIG. 1. Introduction to imaging type-I and type-II domain regions with Lorentz phase microscopy (LPM). (a) Definition of the type-I and type-II DWP structure with corresponding schematics of their expected Lorentz and phase image contrast. The derivative relationships between the phase, magnetic induction, and Lorentz intensity are displayed from the overfocus imaging condition. The calculated line-profiles were carried out using an extension of Eq. (2) that accommodates 360° domains. (b) Micromagnetic simulations of type-I and type-II domains with corresponding Lorentz contrast simulations (369 μm) performed with MUMAX and MALTS, respectively. For all simulations, the input parameters match either measured or calibrated values. The kink in the type-II DWP phase line scan corresponds to the DWP out-of-plane core. (c) Schematic of the Co/Pd, $N = 30$ sample studied in this work. (d) Experimental demonstration of the contrast generated by the four possible domain configurations showing the difference images and phase contrast for type-I and type-II domain regions. The blue and red circular arrows designate right- and left-handed Bloch chirality.

The phase shift of an infinitely long domain wall that has no stray fields can be calculated from direct integration of the Bloch component, and it turns out to be

$$\varphi(x; w, \eta) = -2N\cos(\eta)\arctan\left(\tanh\frac{x}{2w}\right), \tag{4}$$

where $N = \pi B_0 t w/\phi_0$ is the number of flux quanta $\phi_0 = 2.07 \times 10^{-15}\,\mathrm{T\,m^2}$ carried by the Bloch component. Equation (4) describes a smooth phase jump of $N\pi\cos(\eta)$ radians across the domain wall. Therefore, a type-I DWP will appear as a peak in the phase image, bright or dark depending on the chirality, while a type-II DWP will appear as a double-jump, as shown in Fig. 1(a) (sketch), 1(b) (simulated), and 1(d) (experimental).

Imaging type-II DWPs is experimentally challenging due to the small separation between the pair of domain walls, and the relatively narrow defocus range available such that the contrast overlap and the signal-to-noise issues are limited. Raw out-of-focus images are shown in supplemental Fig. 4, where the contrast is barely visible, making the interpretation and the analysis troublesome [52]. To overcome this problem, we acquired images at equidistant defocus (over/under) and used careful cross-correlation to obtain difference (underfocus minus overfocus) images. As a result, the signal-to-noise level is greatly enhanced from the combined effects of doubling of LPM intensity and background subtraction. Figure 2 shows difference images acquired at varying defocus where both type-I and type-II domain regions can be observed. Visible in the profiles shown in Fig. 2(c), type-II contrast varies greatly

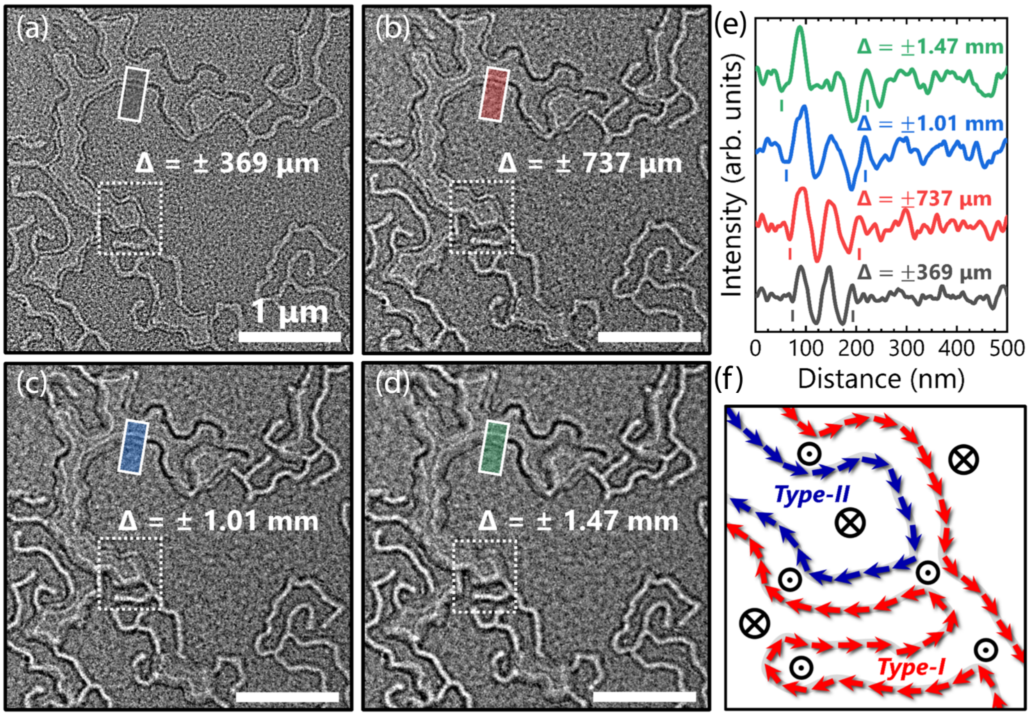

FIG. 2. Fresnel contrast of type-II 360° domain regions. (a)–(d) Difference images of a representative region that contains both type-I and type-II regions acquired at varying defocus magnitude. There is a noticeable jump in the background contrast level from the area between two type-II DWPs. (e) Line scans of the difference image intensity to show the contrast overlap that occurs as the defocus is increased. The broadening of the apparent domain width is designated with colored lines. All difference, phase, and induction images in the following figures were acquired at a defocus magnitude of 369 μm. (f) Schematic that demonstrates the type-I to type-II DMP spin structure transition that can be derived from the difference image contrast.

as a function of defocus. At the lowest defocus, 369 μm, the expected bright-dark contrast from each domain wall is resolved with limited contrast overlap. As the defocus of the difference images is increased, the contrast begins to overlap due to the expected broadening of the domain-wall contrast with increased defocus [17]. This leads to a reduction of the central peak intensity as they are of opposite sign, and it restricts accurate phase retrieval and reconstruction using TIE. At the highest defocus shown, the central contrast is almost completely negated, rendering interpretation difficult [50]. The influence of defocus on the phase retrieval of type-I and type-II DWPs is shown in supplemental Fig. 5 [52].

Type-II domain regions produce a distinctive contrast and are clearly observed upon nucleation, following a reduction of the applied field from saturation, and they form over large areas in a variety of configurations, as shown in Fig. 3. From the difference image and phase image, type-I regions cover the majority of the image shown where both left-handed and right-handed chiralities are apparent. For each type-I chirality, there is a corresponding type-II domain that can form within its areal coverage. Focusing on the phase image in Fig. 3(b), it appears that the preferred formation mechanism of a type-II domain region is via bifurcation of a type-I domain (highlighted with red arrows in the phase image) that inevitably returns to the original type-I chirality through the formation of two π-BLs. Other formation mechanisms of type-II domain regions with less prevalence are highlighted with a blue and green arrow in Fig. 3(c). The spatial extent and prevalence of type-II domains shown in Fig. 3 warrant further investigation to understand the evolution and role that type-II domains and BLs play in skyrmion formation.

To model phenomenologically a BL, we consider a magnetization unit vector describing a 180° Bloch wall that gradually switches its chirality from left- to right-handed along its length, over the same wall-width distance w as the Bloch component itself,

$$\mathbf{m}(x, y; w) = \left\{\operatorname{sech}\left(\frac{y}{w}\right)\operatorname{sech}\left(\frac{x}{w}\right),\right.$$
$$\left.\tanh\left(\frac{y}{w}\right)\operatorname{sech}\left(\frac{x}{w}\right), \tanh\left(\frac{x}{w}\right)\right\}. \qquad (5)$$

By adding a second Bloch domain wall with fixed chirality at a distance $W > 5\,w$, we obtain a model for the transition between a type-I and a type-II DWP, which contains a BL. The Lorentz contrast, phase shift, and colored phase gradient map are shown in Figs. 4(a), 4(c), and 4(e), respectively, and they can be compared to their experimental counterparts in Figs. 4(b), 4(d), and 4(f). The simulations reproduce all visible image features: (i) Lorentz contrast switching from a single to a double peak as the type-I region turns into a type-II region [compare Figs. 4(a) and 4(b)], and the fingerprint of the BL contrast, a bright-dark (or dark-bright, depending on the chirality) globule, slightly tilted, where the Bloch component vanishes; (ii) the two phase levels (high-low-high) of type-I's, versus the three phase levels of type-II's (higher-high-low), and the phase gradient connected to type-II domains [compare Figs. 4(c) and 4(d)]; and (iii) the "flair" protruding from

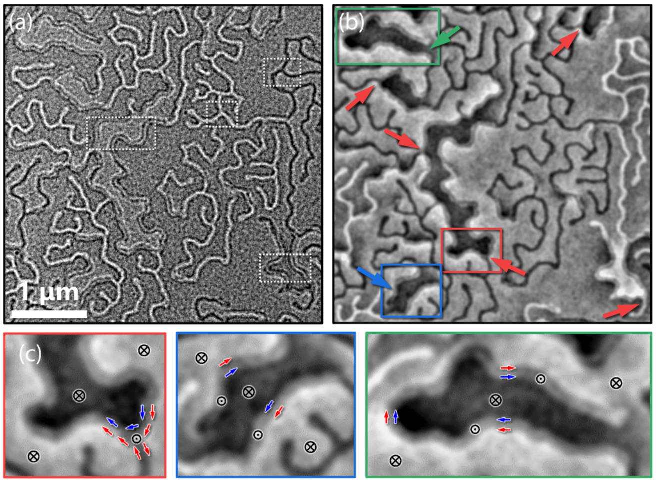

FIG. 3. Shown is the prevalence and preferential formation mechanism of type-II domain regions. (a) Difference images of a typical state observed from the Co/Pd $N = 30$ sample upon lowering the applied field from a saturated state. The applied field is 306 mT, where the white boxes correspond to the type-I and type-II examples in Fig. 1(d). (b) Phase image identifying the preferential formation of type-II domain regions through bifurcation of a type-I domain that are designated by red arrows, with other formation pathways highlighted by a blue and green arrow. Part (c) shows enlarged examples of the variations of type-II domain regions. The first, highlighted in red, demonstrates the formation of a type-II domain through bifurcation of a type-I domain. For the region highlighted in green, a single type-II domain folds over itself while the region highlighted by the blue arrow demonstrates a type-II region that forms in unattached, neighboring domains. Pair formation of type-II domain regions is observed for all large-area cases.

the BL, generated by the local increase in the Néel component, and its stray field spreading outward in the surrounding region, evidenced by the blue-green shade fanning out [compare Figs. 4(e) and 4(f)]. In the BL shown in Fig. 4(e) and imaged in Fig. 4(f), the chirality of the wall progresses from $-1(\eta = \pi)$ to $0(\eta = \pi/2)$ to $+1(\eta = 0)$, along its length from bottom to top. The color of the flair is a direct indication of the sign of the local Néel component and hence of the left- or right-handedness of the structure. A slightly more complicated scenario is shown at the bottom of Fig. 4, where we considered two BLs from two DWPs facing each other. The comparison between Figs. 4(k) and 4(l), in particular the shade of green visible in the area between the two DWPs that is highlighted with gray arrows in Fig. 4(k), reveals clearly that the two BLs interact magnetostatically via their stray fields, and they can either attract or repel each other depending on their chirality, which is discussed subsequently.

To further investigate the evolution, persistence, and influence of type-II DWPs on the skyrmion formation process, type-II domain regions were tracked systematically from initial nucleation (∼310 mT) to near zero field (11 mT), and then to skyrmion formation and type-II domain annihilation (∼523 mT). The full image sequence can be seen in Fig. 5. From the first image at 310 mT, two type-II domain regions can be readily observed—one that formed through the bifurcation of two type-I domains (red box), and one that forms within a singular type-I domain where the type-II domain region folds over itself (blue box). Notably, the BL pair dynamics from these two type-II regions is divergent and is focused on in Fig. 5(b), where the white arrows indicate the positions of the BLs. For the type-II region highlighted with the blue box, the BLs are repulsive in response to a reduction in applied field, while for the region highlighted with the red box, the BLs converge closer together. This confirms that the interaction between BLs is diverse in character, and it emphasizes the need to resolve the exact structure of BL pairs, which was initially investigated by Grundy *et al.* [55],

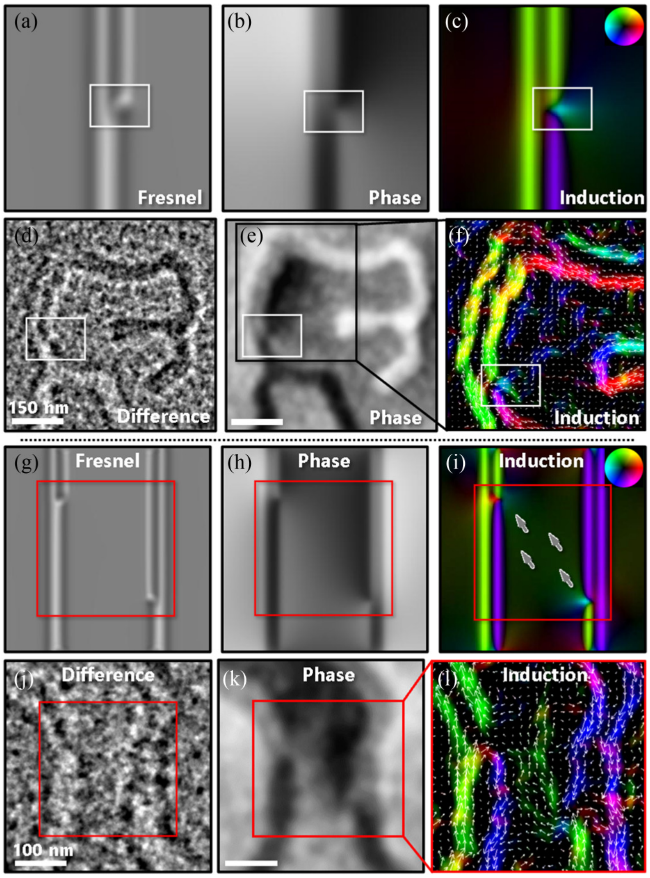

FIG. 4. Demonstration of the connection between BLs and stray fringing fields for two situations. (a), (c), (e) Simulated Fresnel, phase, and colored phase gradient images from a BL in a DWP turning from type-I (bottom) to type-II (top); (b), (d), (f) corresponding experimental images. For this case, the flux protruding from the BL is clearly resolved in the form of a “flair” at the bottom left corner of (f), and in agreement with the simulation in (e). The location of the BL is highlighted with a white box. (g), (i), (k) Simulated Fresnel, phase, and colored phase gradient images from two DWPs facing each other, each containing a BL, and each transitioning from type-I to type-II, although at different positions along their length; (h), (j), (l) corresponding experimental images. The areas of interest for comparison are highlighted with a red box. Note in this case the opposite color of the two BL flairs, blue on the right, red on the left, in agreement with the experimental image and denoting opposite chirality. Also notice the weak green shade of the region inside the two DWPs that is emphasized with gray arrows, reflecting the stray field established between the BLs, also clearly visible in the experimental image.

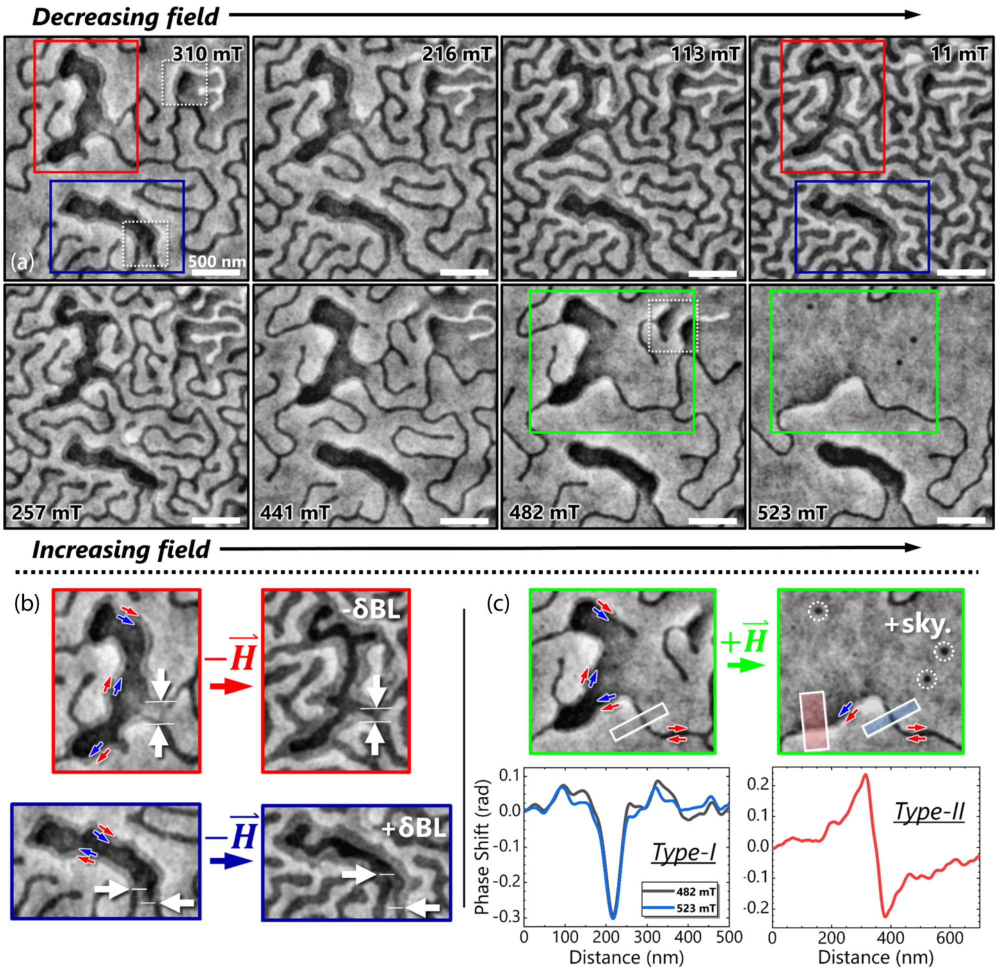

FIG. 5. An investigation of the persistence and evolution of type-II domain regions. A phase image series acquired on the same area shows that type-II domain regions form early in the nucleation process and persist to high applied fields where skyrmion nucleation occurs. Further, it reveals the distinct and varied dynamic nature of the BL pair interaction, which is focused on in (b). The white box in the image from 310 mT designates the areas displayed in Fig. 4, while the white box in the 482 mT image designates the area displayed in Fig. 5. (b) The red and blue boxes in the phase image from 310 mT highlight two different type-II domain regions. The white arrows indicate the location of the BLs essential for the formation of a type-II domain. As the field is decreased, the BL pairs are dynamic with an attractive character displayed by the region highlighted with the red box and a repulsive character shown in the region highlighted with the blue box. Part (c) demonstrates the behavior of type-II domain regions at high applied fields where skyrmion formation occurs. At the highest applied field (523 mT), skyrmion (sky.) nucleation is observed and, further, it shows an unpaired type-II domain that enables direct comparison with the simulation shown in Fig. 1(b). Line scans of type-I domain regions confirm the consistency of the retrieved phase, while the line scan of the type-II domain agrees with the phase gradient surrounding type-II domains.

recently investigated through simulation by Cheng *et al.* [34], and in the current work. Figure 5(c) focuses on an annihilation mechanism of a type-II domain region, and it shows that type-II's are active agents in the formation of skyrmions. Both type-II domain regions survive through the evolving field with limited change to their overall shape, and they persist to high applied fields where skyrmion formation occurs.

In Fig. 5(c), a type-II domain region that lost its complementary DWP is observed, allowing for comparison to the simulated phase shift of a type-II domain. It is found from the experimental profiles that, from the type-I region, consistent phase shifts can be retrieved for varied fields and, significantly, the retrieved phase from the type-II region agrees qualitatively with the simulated phase shift in Fig. 1(b) and also with the more extensive simulations performed in Fig. 4, supporting that type-II DWPs are accompanied by stray fringing fields. This is further emphasized in Fig. 6, which highlights a region where the domain walls of neighboring type-II DWPs are oriented in the same direction. From the profile in Fig. 6(c), there is a clear phase gradient between the two aligned type-II regions that is strong evidence of a stray field interaction between the type-II DWPs and their BLs. In Fig. 6(d), the magnetic induction map from this area is shown with an accompanying schematic in Fig. 6(e). It is seen that stray field interactions are aligned opposite to the domain-wall orientation, and that the interaction between BLs serves as a stabilizing mechanism for type-II regions, in agreement with findings from Figs. 4(g)–4(l) and investigated as a function of q_0 in supplemental Fig. 6 [52]. Indeed, a phase gradient is found for all phase images and simulations of type-II DWPs analyzed in this work, and it highlights previously unresolved domain stabilization mechanisms that play a role in thick

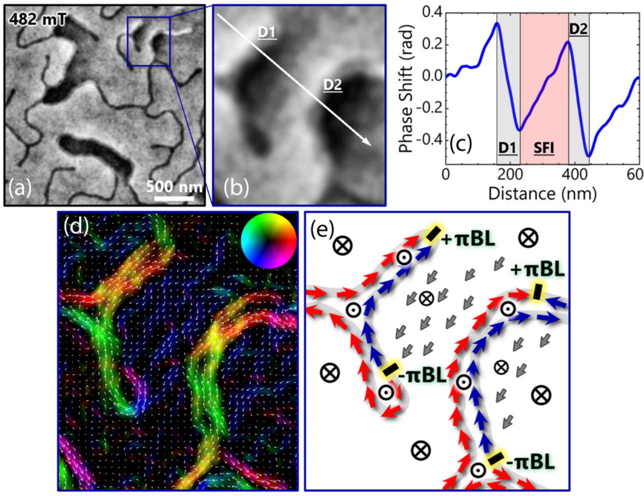

FIG. 6. Illuminating interactions that can occur between BL pairs. (a) Phase image acquired at 482 mT showing the interactions between type-II domains and BLs that is also displayed as part of Fig. 4. (b) Enlarged image of the area of interest in (a). (c) Line scan acquired from the region shown with a white dotted line in Fig. 4(b). There is a clear phase gradient between the two domains (D1, D2), which corresponds with a stray field interaction (SFI) shown in (d). Induction map with a corresponding schematic in (e) of the region highlighted by the blue boxes in (a). The gray arrows indicate regions where there is an electron phase gradient and reveals interactions that can occur between BL pairs and type-II domains.

DMI multilayer systems and in skyrmion formation, discussed subsequently.

Figure 7 investigates the role that type-II DWPs play on the nucleation of skyrmions at high applied fields with an expanded image set shown in Fig. 7 of the Supplemental Material [52]. From the highlighted red and blue boxes, it is observed that upon annihilation, type-II domains can nucleate mixed-character skyrmions. The nucleation of a type-I skyrmion from a type-II DWP is further supported by supplemental movies S1, S2, and S3, which depict the relaxation of a type-II domain region and show the dynamic nature of BLs in response to changing fields as well as the nucleation of a type-I skyrmion from a type-II DWP. Micromagnetic simulations on the Bloch/Néel mixed domain-wall structure present in the investigated thin film are shown in supplemental Fig. 8 [52]. Interestingly, the type-II DWPs highlighted in the red and blue boxes in Fig. 7 are of the same structure, yet the Bloch components of the stabilized mixed-character skyrmions are of opposite chirality. This, in combination with the identification of type-II domains and the interaction between BL pairs that can form, suggests that there are additional energies that can impact skyrmion formation and skyrmion chirality. For the formation of a BL and type-II DWP to be energetically favorable, there must be local and/or long-range energies that balance the additional cost to the exchange energy. In fact, Lemesh *et al.* recently reported that the presence of type-II DWPs and BLs [34] does coincide with the formation of complex stray field interactions and additional magnetostatics terms [31]. Despite investigations of the energy of BL formation in relation to bubble material physics [21,22,25,55], albeit without a DMI, and recently by Krizakova *et al.* [32] in relation to domain-wall propagation, the energetics of BLs, including their interactions and their influence on skyrmion formation, remain unknown. We emphasize that it is imperative to resolve and theoretically model the fine structure and interactions of topological spin textures at the nanoscale to validate assumptions.

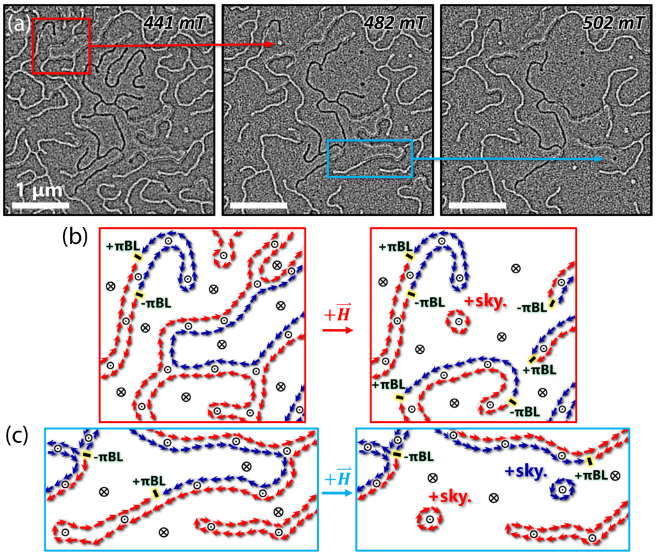

FIG. 7. Probing the role that type-II domain regions play on skyrmion formation. (a) Difference images acquired from the same area at high fields where skyrmion nucleation occurs. An expanded image series on skyrmion nucleation is shown in the Supplemental Material. The red and blue boxes highlight type-II domains that nucleate skyrmions upon increased applied field and type-II DWP annihilation. Parts (b) and (c) show schematic representations of the difference images shown in (a). The type-II domains are of the same structure, yet they nucleate skyrmions of opposite chirality, which suggests there are additional energetics that can influence skyrmion chirality in mixed-character DMI multilayer thin films.

III. CONCLUSION

In summary, we utilize advanced Lorentz phase microscopy based on the transport-of-intensity analysis to reveal previously unreported domain configurations, the pair formation of BLs, and their interactions. We show that type-II domain regions preferentially form through the bifurcation of a single type-I domain that necessitates the formation of BL pairs. Type-II regions form early in the nucleation process from a saturated state and persist to high applied fields where skyrmions are stabilized. Moreover, it is established that BLs can be dynamic upon changes to the spin state without impacting the stability of the domain. Significantly, we demonstrate that BL pairs interact strongly via their stray field, which facilitates the stability of a type-II domain. Further, type-II domain regions play a role in skyrmion formation and can nucleate mixed-character skyrmions of either right- or left-handed chirality. We emphasize that unresolved energetics plays a substantial role in DMI multilayer thin film and is of timely importance to calculate theoretically and resolve experimentally, including for antiskyrmions, bimerons, and other exotic spin textures.

ACKNOWLEDGMENTS

This research was supported by the U.S. Department of Energy, Office of Basic Energy Sciences, Division of Materials Science and Engineering, under Contract No. DE-SC0012704. The work at National University of Singapore was supported by the National Research Foundation (NRF), Prime Minister's Office, Singapore, under its Competitive Research Programme (CRP Award No. NRFCRP12-2013-01).

The authors declare no competing financial interests.

---

[1] M. J. Benitez, A. Hrabec, A. P. Mihai, T. A. Moore, G. Burnell, D. McGrouther, C. H. Marrows, and S. McVitie, Nat. Commun. **6**, 8957 (2015).

[2] S. Woo, K. Litzius, B. Krüger, M.-Y. Im, L. Caretta, K. Richter, M. Mann, A. Krone, R. M. Reeve, M. Weigand, P. Agrawal, I. Lemesh, M.-A. Mawass, P. Fischer, M. Kläui, and G. S. D. Beach, Nat. Mater. **15**, 501 (2016).

[3] A. Soumyanarayanan, M. Raju, A. L. Gonzalez Oyarce, A. K. C. Tan, M.-Y. Im, A. P. Petrović, P. Ho, K. H. Khoo, M. Tran, C. K. Gan, F. Ernult, and C. Panagopoulos, Nat. Mater. **16**, 898 (2017).

[4] S. D. Pollard, J. A. Garlow, J. Yu, Z. Wang, Y. Zhu, and H. Yang, Nat. Commun. **8**, 14761 (2017).

[5] S. Parkin and S.-H. Yang, Nat. Nanotechnol. **10**, 195 (2015).

[6] R. Tomasello, E. Martinez, R. Zivieri, L. Torres, M. Carpentieri, and G. Finocchio, Sci. Rep. **4**, 6784 (2015).

[7] D. Maccariello, W. Legrand, N. Reyren, K. Garcia, K. Bouzehouane, S. Collin, V. Cros, and A. Fert, Nat. Nanotechnol. **13**, 233 (2018).

[8] S. Emori, U. Bauer, S.-M. Ahn, E. Martinez, and G. S. D. Beach, Nat. Mater. **12**, 611 (2013).

[9] W. Jiang, X. Zhang, G. Yu, W. Zhang, X. Wang, M. Benjamin Jungfleisch, J. E. Pearson, X. Cheng, O. Heinonen, K. L. Wang, Y. Zhou, A. Hoffmann, and S. G. E. te Velthuis, Nat. Phys. **13**, 162 (2017).

[10] X. Z. Yu, N. Kanazawa, W. Z. Zhang, T. Nagai, T. Hara, K. Kimoto, Y. Matsui, Y. Onose, and Y. Tokura, Nat. Commun. **3**, 988 (2012).

[11] K. Litzius, I. Lemesh, B. Krüger, P. Bassirian, L. Caretta, K. Richter, F. Büttner, K. Sato, O. A. Tretiakov, J. Förster, R. M. Reeve, M. Weigand, I. Bykova, H. Stoll, G. Schütz, G. S. D. Beach, and M. Kläui, Nat. Phys. **13**, 170 (2017).

[12] S. Woo, K. M. Song, X. Zhang, Y. Zhou, M. Ezawa, X. Liu, S. Finizio, J. Raabe, N. J. Lee, S.-I. Kim, S.-Y. Park, Y. Kim, J.-Y. Kim, D. Lee, O. Lee, J. W. Choi, B.-C. Min, H. C. Koo, and J. Chang, Nat. Commun. **9**, 959 (2018).

[13] W. Legrand, D. Maccariello, F. Ajejas, S. Collin, A. Vecchiola, K. Bouzehouane, N. Reyren, V. Cros, and A. Fert, Nat. Mater. **19**, 34 (2020).

[14] W. Legrand, J.-Y. Chauleau, D. Maccariello, N. Reyren, S. Collin, K. Bouzehouane, N. Jaouen, V. Cros, and A. Fert, Sci. Adv. **4**, eaat0415 (2018).

[15] Y. Dovzhenko, F. Casola, S. Schlotter, T. X. Zhou, F. Büttner, R. L. Walsworth, G. S. D. Beach, and A. Yacoby, Nat. Commun. **9**, 2712 (2018).

[16] I. Lemesh and G. S. D. Beach, Phys. Rev. B **98**, 104402 (2018).

[17] J. A. Garlow, S. D. Pollard, M. Beleggia, T. Dutta, H. Yang, and Y. Zhu, Phys. Rev. Lett. **122**, 237201 (2019).

[18] K. Fallon, S. McVitie, W. Legrand, F. Ajejas, D. Maccariello, S. Collin, V. Cros, and N. Reyren, Phys. Rev. B **100**, 214431 (2019).

[19] A. P. Malozemoff and J. C. Slonczewski, Phys. Rev. Lett. **29**, 952 (1972).

[20] J. C. Slonczewski, Phys. Rev. Lett. **29**, 1679 (1972).

[21] J. C. Slonczewski, J. Appl. Phys. **45**, 2705 (1974).

[22] A. P. Malozemoff, Appl. Phys. Lett. **21**, 149 (1972).

[23] A. Rosencwaig, W. J. Tabor, and T. J. Nelson, Phys. Rev. Lett. **29**, 946 (1972).

[24] J. C. Slonczewski, A. P. Malozemoff, and O. Voegeli, AIP Conf. Proc. **10**, 458 (1973).

[25] A. Hubert, AIP Conf. Proc. **18**, 178 (1974).

[26] S. Konishi, IEEE Trans. Magn. **19**, 1838 (1983).

[27] S. Konishi, K. Matsuyama, I. Chida, S. Kubota, H. Kawahara, and M. Ohbo, IEEE Trans. Magn. **20**, 1129 (1984).

[28] F. Humphrey and J. Wu, IEEE Trans. Magn. **21**, 1762 (1985).

[29] D. Klein and J. Engemann, J. Appl. Phys. **57**, 4071 (1985).

[30] T. Suzuki, H. Asada, K. Matsuyama, E. Fujita, Y. Saegusa, K. Morikawa, K. Fujimoto, M. Shigenobu, K. Nakashi, H. Takamatsu, Y. Hidaka, and S. Konishi, IEEE Trans. Magn. **22**, 784 (1986).

[31] I. Lemesh and G. S. D. Beach, Phys. Rev. Appl. **12**, 044031 (2019).

[32] V. Krizakova, J. P. Garcia, J. Vogel, N. Rougemaille, D. de Souza Chaves, S. Pizzini, and A. Thiaville, Phys. Rev. B **100**, 214404 (2019).

[33] Y. Yoshimura, K.-J. Kim, T. Taniguchi, T. Tono, K. Ueda, R. Hiramatsu, T. Moriyama, K. Yamada, Y. Nakatani, and T. Ono, Nat. Phys. **12**, 157 (2016).

[34] R. Cheng, M. Li, A. Sapkota, A. Rai, A. Pokhrel, T. Mewes, C. Mewes, D. Xiao, M. De Graef, and V. Sokalski, Phys. Rev. B **99**, 184412 (2019).

[35] S. R. Herd and P. Chaudhari, Phys. Status Solidi **18**, 603 (1973).

[36] P. J. Grundy and S. R. Herd, Phys. Status Solidi **20**, 295 (1973).

[37] S. R. Herd, Phys. Status Solidi **38**, 305 (1976).

[38] N. D. Khanh, T. Nakajima, X. Yu, S. Gao, K. Shibata, M. Hirschberger, Y. Yamasaki, H. Sagayama, H. Nakao, L. Peng, K. Nakajima, R. Takagi, T. Arima, Y. Tokura, and S. Seki, Nat. Nanotechnol. **15**, 444 (2020).

[39] T. Hishii, S. Matsushita, and Y. Sakurai, Jpn. J. Appl. Phys. **16**, 1467 (1977).

[40] A. K. Nayak, V. Kumar, T. Ma, P. Werner, E. Pippel, R. Sahoo, F. Damay, U. K. Rößler, C. Felser, and S. S. P. Parkin, Nature (London) **548**, 561 (2017).

[41] M. Beleggia, M. A. Schofield, V. V. Volkov, and Y. Zhu, Ultramicroscopy **102**, 37 (2004).

[42] M. De Graef and Y. Zhu, J. Appl. Phys. **89**, 7177 (2001).

[43] X. Zhang and Y. Oshima, Microscopy **64**, 395 (2015).

[44] M. Beleggia and Y. Zhu, Philos. Mag. **83**, 1045 (2003).

[45] M. Beleggia, Y. Zhu, S. Tandon, and M. De Graef, Philos. Mag. **83**, 1143 (2003).

[46] S. McVitie and D. T. Ngo, J. Phys. Conf. Ser. **126**, 012041 (2008).

[47] C. T. Koch, Ultramicroscopy **108**, 141 (2008).

[48] M. Mitome, K. Ishizuka, and Y. Bando, J. Electron Microsc. (Tokyo) **59**, 33 (2010).

[49] C. T. Koch and A. Lubk, Ultramicroscopy **110**, 460 (2010).

[50] J. Cui, Y. Yao, X. Shen, Y. G. Wang, and R. C. Yu, J. Magn. Magn. Mater. **454**, 304 (2018).

[51] C. T. Koch, Micron **63**, 69 (2014).

[52] See Supplemental Material at http://link.aps.org/supplemental/10.1103/PhysRevB.102.214429 for a methods section, further details on the procedure for electron phase retrieval, extended data, and micromagnetic simulations to support the main text.

[53] A. Vansteenkiste, J. Leliaert, M. Dvornik, M. Helsen, F. Garcia-Sanchez, and B. Van Waeyenberge, AIP Adv. **4**, 107133 (2014).

[54] S. K. Walton, K. Zeissler, W. R. Branford, and S. Felton, IEEE Trans. Magn. **49**, 4795 (2013).

[55] P. J. Grundy, D. C. Hothersall, G. A. Jones, B. K. Middleton, and R. S. Tebble, Phys. Status Solidi **9**, 79 (1972).

Correction: An incorrect version of Figure 1(b) was used for publication and has now been replaced with the corrected version.